Electronic Supplementary Material (ESI) for Lab on a Chip.

PROTEINACEOUS MICROSTRUCTURE IN A CAPILLARY:

A STUDY OF NON-LINEAR BENDING DYNAMICS

Mario Marini[a,§], Amirbahador Zeynali[a,§], Maddalena Collini[a,c], Margaux Bouzin[a], Laura Sironi[a,c], Laura D'Alfonso[a,c], Francesco Mantegazza[b,c], Valeria Cassina[b,c], Giuseppe Chirico[a,c,*]

[a] Dipartimento di Fisica, Università degli Studi di Milano-Bicocca, Piazza della Scienza 3, 20126, Milano (I)

[b] Dipartimento di Medicina e Chirurgia, Università degli Studi di Milano-Bicocca, Via Follereau 3, 20854, Vedano al Lambro (I)

[c] Bionanomedicine Center, BIONANOMIB, Via Follereau 3, 20854, Vedano al Lambro (I)

§ contributed equally to the work

*giuseppe.chirico@unimib.it

SUPPLEMENTARY INFORMATION

Sommario

1. Optical setup

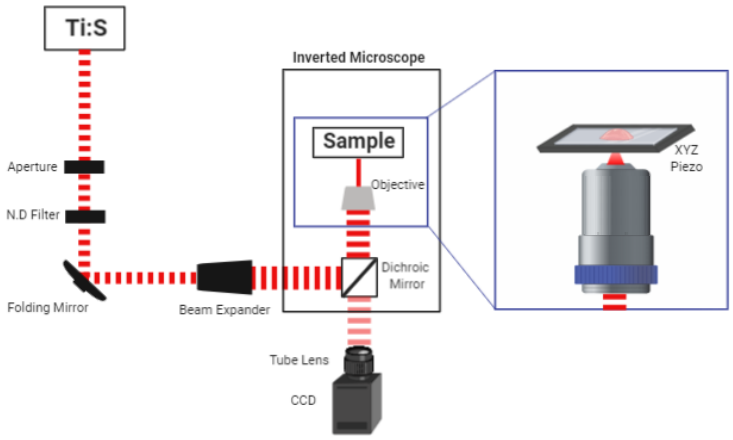

***Fig. SI1: optical setup**. Two-Photon Absorption (TPA) Additive Optical Manufacturing (AOM) setup exploiting a tunable Ti:Sa femtosecond pulsed laser (wavelength 800 nm, repetition rate 80MHz, 250 fs pulse width). The beam is focused on the sample by an inverted TE-300 Nikon microscope, mounting a water-immersion objective (Olympus LUMFI 60X, N.A. 1.1, 1.5 mm working distance). The sample is scanned by means of a 3-axis piezo actuator (Hera P733 for xy scanning, Pifoc-P725 for z scanning).*

2. Test of the continuity of the flow induced by the microfluidic pump

Capillaries with square 800x800 μm^2 inner cross-section (CMScientific Ltd., UK) were connected to a syringe pump (NE-300, KF-Technologies, I). We used a larger cross-section capillary than the one used for the experiments in the main text (300x300 μm^2) in order to reduce the flow speed by a factor of approximately 0.14 times and be able to detect the motion of flowing objects by the laser-scanning microscope (Leica TCS SP5, Leica Microsystems, D) with a 8-kHz line scan frequency. The continuity of the volumetric flow induced by the syringe pump was evaluated by analyzing the flow of fluorescent microbeads (1 μm in size) in the microcapillary. The motion was captured by means of repeated line scan on the confocal microscope along the direction of the flow (in the middle of the channel, along the channel axis).[1] The acquired data were composed in the form of XT carpet images, where the horizontal X axis is the scan axis (here 512 pixels, with pixel size 135 nm) and the vertical T axis is the time axis (here 8192 pixels, separated by τ_f=125 μs). While immobile particles appear in XT images as vertical lines, any line appearing in the XT frame as slanted by an angle θ with respect to the X axis corresponds to a particle moving with speed v uniform in time. The speed can be measured graphically from the angle θ as $v = \delta x/(tg(\theta)\tau_f)$, where τ_f (here 125 μs) is the spacing of the rows along the T- axis and δx is the pixel size (here 125 nm, see **Fig. SI2**). Quantitatively, the speed of flowing particles can also be measured by means of image correlation

spectroscopy with the SLIC method[2], by exploiting the computation of the cross-correlation function between pairs of columns in the XT-image.

We have acquired for each pump flow rate a set of ten 512x8192 XT images M_{XT}, each spanning a total scanning time of 1.024 s for an overall test of the flow of about 10 s. The test was performed both right after the pump flow was set and at the equilibrium, 3 s after the pump flow was switched on. First, we notice that oscillations in the pump pressure at times shorter than 1 s (i.e., frequency larger than 1 Hz) should give rise to wavy slanted lines in the acquired XT frames. These wavy slanted lines are visible only for a pump volumetric flow rate Q lower than 0.03 mL/Min (**Fig. SI2**), which is one order of magnitude lower than the one used in the experiments reported in the main text.

For a more quantitative measurement of the flow speed on XT images over longer time scales by the SLIC method, we computed the cross-correlation between pairs of columns, $\{M_{xt}[:,i]\}_{i\,=\,1,..N}$ and $\{M_{xt}[:,i+k]\}_{i\,=\,1,..N}$, spaced by k pixels, corresponding to a spatial lag $\Delta x = k\,\delta x$. The span along the T axis is determined by the number of rows employed for the computation of the cross-correlation function. Here, we have used N=1024 rows, corresponding to a time span $\Delta T = N\tau_f$=128 ms. This is our time resolution for the measurement of the flow speed. When the flow speed is uniform over the time stretch ΔT, the slanted lines in the carpet images have a single slope (**Fig. SI2** for Q $\geq$ 0.09 mL/min). This corresponds to the presence of a single peak in the cross-correlation function (**Fig. SI3**), whose peak lag time, τ_{max}, increases linearly with the lag space Δx. From the slope of the Δx-versus-τ_{max} linear plot, we compute the flow speed on the time stretch ΔT. In order to directly relate this measurement with the corresponding speed value in the 300x300 μm^2 capillary used for the measurement of the bending dynamics, we divided the slope of the plot of Δx as a function of τ_{max} by a factor $\left(\frac{300}{800}\right)^2 \cong 0.14$, thereby retrieving what is plotted as v_{300} in **Fig. SI3B,C**. For volumetric flow rates smaller than 0.03 mL/min, the presence of fluctuations in the pump flow rate (**Fig. SI2**) results in double-peaked cross-correlation functions (**Fig. SI3A**, inset). As a matter of fact, while the single-peak cross-correlation function (**Fig. SI3A**) can be well described by a Gaussian function, the double-peak cross-correlation measured for Q=0.03 mL/min (**Fig. SI3A**, inset) cannot. From the analysis of the cross-correlation, one could then derive two values of τ_{max} for the same space lag Δx, thereby recovering two values of the flow speed. However, since the change of the flow speed appears to be continuous between two extreme values, their measurement can only be taken as a qualitative estimate.

For volumetric flow rates larger than 0.09 mL/min, more than three times lower than the volumetric rates used in the bending dynamics experiments, we cannot detect any clear oscillation in the range of frequency 0.5-3 Hz (**Fig. SI3C**) at least 3 seconds after the onset of the flow. At most, tiny periodic variations of the flow speed can be sometimes detected for frequencies larger than about 4 Hz (**Fig. SI2** and **Fig.SI3B,C**). It is also noteworthy that the actual speed in the channel comes to equilibrium with a jump that occurs in much less than 125 μs (**Fig. SI3B**), followed by a smooth growth with average growth time of about 1.5 $\pm$ 0.3 s. While the sudden jump in the flow speed correlates well with the bending overshoot observed experimentally for microstructures (**Fig.5** in the main text), the smooth speed growth occurs over a timescale that is ten times shorter than the typical tens-of-second bending time measured on microstructures.

Overall, the measurements of **Fig. SI2,3** clearly indicate that the flow speed in the microcapillary is uniform in the range of volumetric flow rates that we have exploited for the bending dynamics experiments reported in the main text.

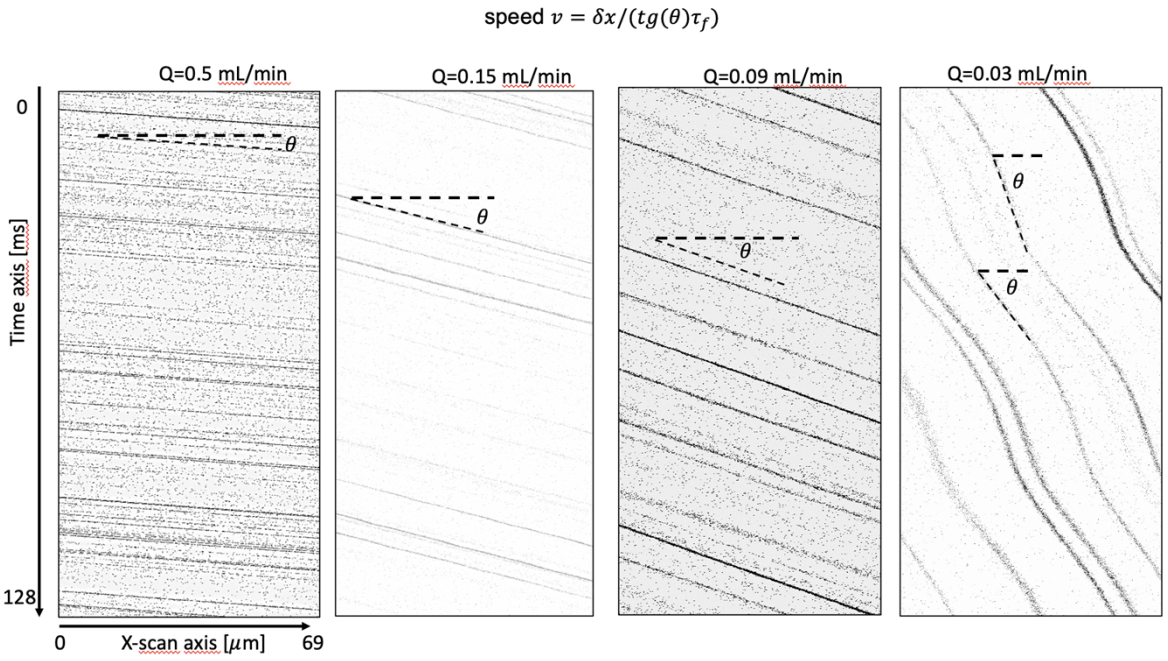

Fig. SI2*: *Test of the continuity of the flow induced by the microfluidic pump (I). *XT carpet images of fluorescent microbeads flowing in an 800x800 µm² microcapillary, acquired in line-scan mode on a Leica TCS SP5 confocal microscope. Flow rates Q from right to left: 0.03 mL/min, 0.09 mL/min, 0.15 mL/min and 0.5 mL/min. Any slanted straight line indicates a particle moving with uniform flow speed. For Q=0.03 mL/min, microbeads undergo an oscillatory motion with a frequency of about 17 Hz, which is much higher than the characteristic oscillation frequencies that have been detected and discussed in the present work. Moreover, the flow rate Q=0.03 mL/min is one order of magnitude lower than the one adopted for the microfluidic experiments reported in the main text.*

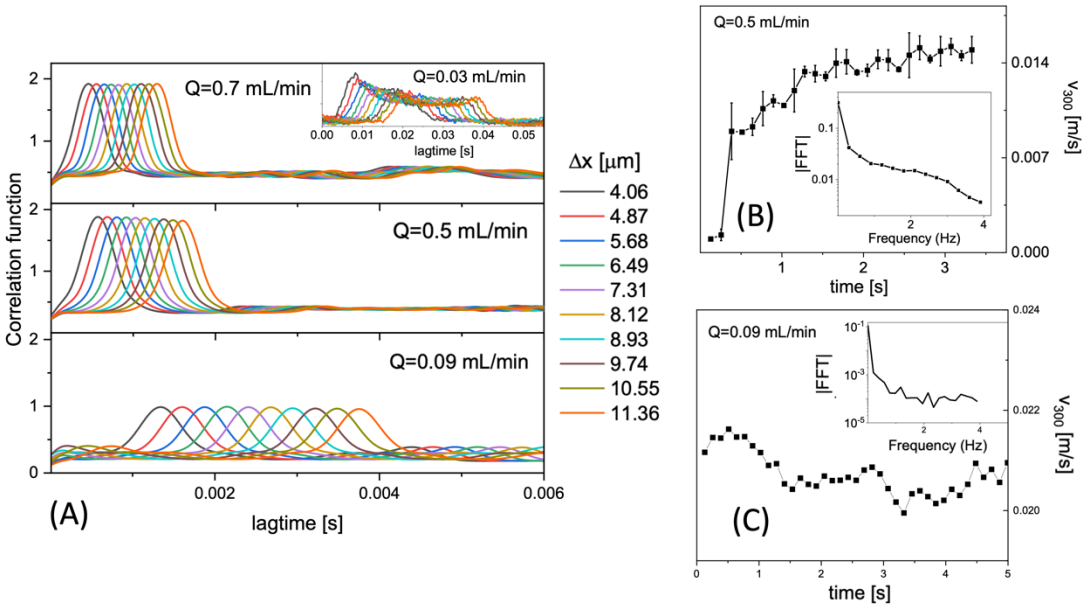

Fig. SI3: Test of the continuity of the flow induced by the microfluidic pump (II). *(A): Cross-Correlation Functions (CCFs) measured between pairs of columns of the XT carpet images (see Fig. SI2) at increasing values of the inter-column distance Δx. CCFs have been computed on stretches of 128 ms along the time axis. The speed of flowing microbeads along the scan axis (parallel to the flow axis) can be recovered from the slope of the space lag Δx as a function of the CCFs peak lagtime. (B), (C): trend of the flow speed (measured on 128-ms time stretches) as a function of time during the flow onset (B) and at the equilibrium (C). Insets report the magnitude of the Fourier spectrum of the flow speed traces.*

3. Calibration of the flow speed in the capillary

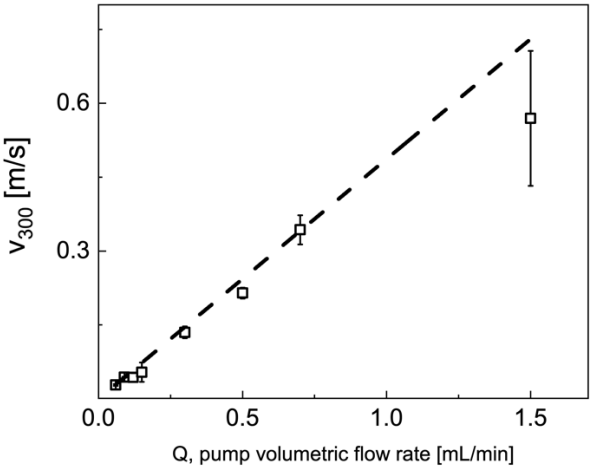

Fig. SI4: Calibration of the flow speed at the center of the capillary as a function of the volumetric flow rate set on the pump*. The speed was measured by acquiring XT images on flowing 1-μm fluorescent beads on the Leica TCS SP5 confocal microscope, and by computing the cross-correlation function between pairs of columns of the XT images at increasing inter-column distance Δx. The*

speed was derived from the linear dependence of the inter-column distance Δx as a function of the peak time τ_{max} of the cross-correlation functions. The speed, quantified in a 800x800 µm² capillary, was finally converted into the corresponding speed v_{300} in a 300x300 µm² capillary according to the decrease in the capillary cross-section. The solid line corresponds to the best fit linear fit of the data with slope 0.48 $\pm\ 0.04\ \frac{m \cdot min}{s \cdot mL}$.

4. Test of the tracking software

In order to track the position of the tip of the microstructures, we exploited the program Tracker provided by the Open Source Physics project (www.compadre.org/osp). The program allows an automatic tracking ("*Autotracker*") of a user defined target in a video in .mp4 or .avi format. *Autotracker* works by creating one or more template images of a feature of interest and then searching in each frame for the best match to that template. The size of the target is a critical parameter. The best match is defined by the highest match score that is computed as the inverse of the sum of the squares of the RGB differences between the template and the image pixels. Once the best match is found, it is compared with nearby match scores to determine an interpolated sub-pixel best match position.

We tested the *Autotracker* tracking algorithm by generating synthetic time-lapse image sequences, mimicking imaging of an object with a shape similar to the tip of a flexible microstructure, where the object is displaced along the x-axis according to an exponential law of the type

$$x = x_0 + \Delta x(1 - exp(-t/\tau)) \qquad (4.1)$$

In order to simulate the effect of the limited spatial resolution of the microscope, we convolved each image with a flat kernel (11 pixels in size) along the vertical (column) direction according to the Python-coded algorithm of **Fig. SI5.** In the sample algorithm of **Fig. SI5**, two edges of a microstructure were simulated at a distance of 30 pixels on an image 256x256 pixels in size. An image 2560x2560 pixel in size was initially employed, and a subsequent ten-time re-bin was applied (note that the algorithm excerpt only reports the simulation of a single row of the image).

An exemplary simulated image is reported in **Fig. SI6**. The simulated video of the resulting displacement of the synthetic microstructure was fed to the Tracker software to track the position of the tip of the structure itself (**Fig. SI6**). We found that a critical parameter for an accurate tracking of the movement is the "evolve rate" parameter, by default set at 20%. This parameter allows the template (which is defined by the user on an initial frame on a feature that is unique and includes high-contrast edges) to evolve during the tracking, so that the template may adapt to shape and

color changes affecting the tracked object along the video. An “evolution rate” of 0% does not evolve at all (constant template image equal to the initial one), whereas an “evolution rate” of 100% completely replaces the template with the match image after each frame. As revealed in **Fig. SI7**, a 20% value for the “evolve rate” parameter is too high to allow an accurate tracking. This can be reached instead by lowering the “evolve rate” parameter to the 7-10% range.

Fig. SI7 also reveals that the tracking algorithm oversamples the spatial coordinates and provides a subpixel resolution that is only slightly affected by the image pixel size. Indeed, discrete position jumps are visible on the retrieved dynamics, no matter the value of the “evolve rate” parameter.

```
import numpy as np

Nframe = 1000                    # number of frames in the simulated movie
N=256                            #number of pixels per row in the image
xrow = np.linspace(0,N*10-1,N*10)  # use a row ten times longer than the final image
tau= 20                          # units seconds, relaxation time
init_pos = 1250                  # in pixels
ss0 = 2000                       # width of the simulated line of the microstructure in a 10x dimension
pos0 = 0                         # position in pixels of the left-most edge of the structure in a 10x dimension
pos1 = 300                       # position in pixels of the right-most edge of the structure in a 10x dimension

for i in range (Nframe):         # build the image row by row

    x = init_pos + (1-np.exp(-i/tau))*100
    row = np.exp(-(xrow)**2/ss0) + np.exp(-(xrow-x-300)**2/ss0)
    row10 = np.zeros((N))

# rebin and rescale the row to the right size = N

    h=0
    for k in np.arange(0,N*10,10):
        row10[h] = row[k:k+10].mean()
        h=h+1
```

Fig. SI5: Image simulation for the test of the tracking software. *We used a Python-coded algorithm to generate simulated images of an object, resembling in shape the microstructures investigated in the present work, displacing along the horizontal axis according to the exponential law of eq. 4.1. Simulated images were convoluted with a flat kernel to take the limited spatial resolution of the laser-scanning confocal microscope into account.*

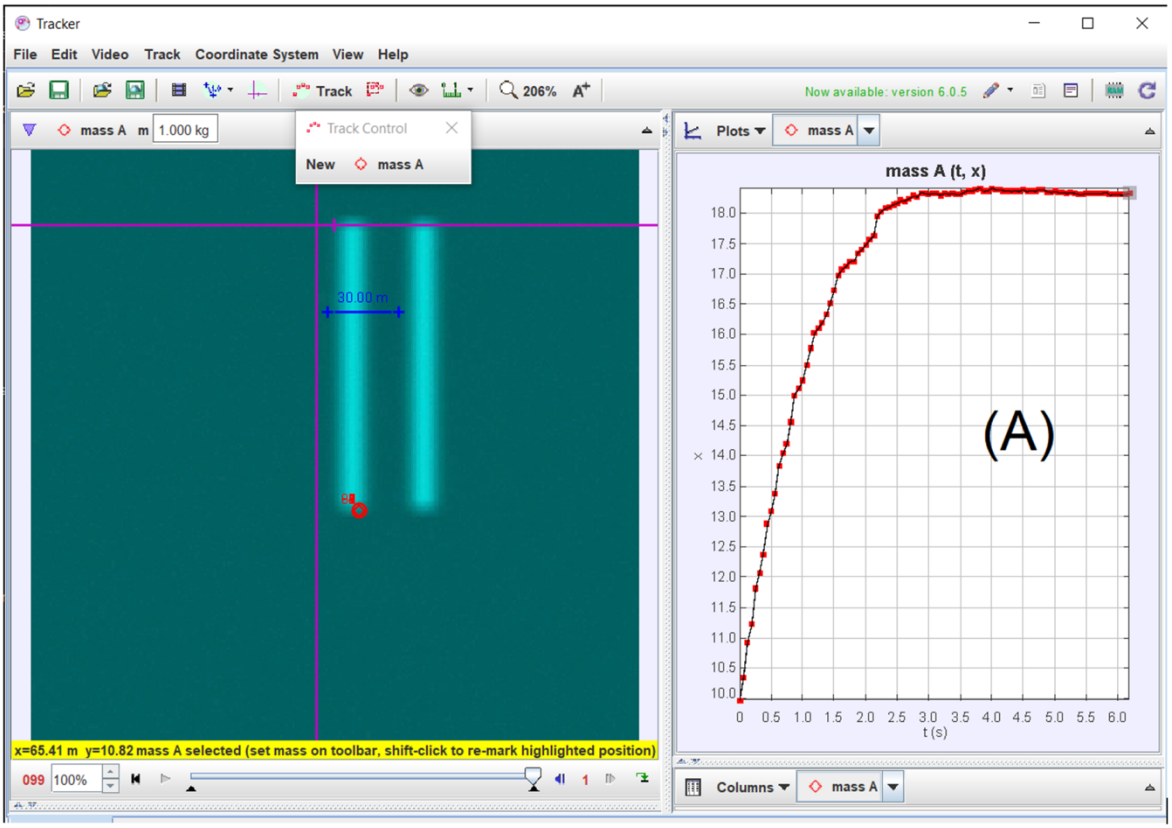

Fig. SI6: Test of the Tracker software (I). *Screenshot of the Tracker program window, showing an exemplary frame of the analyzed image sequence simulating a square cross-section microstructure that displaces according to an exponential law (Eq.4.1) (left) and the result of the structure tip tracking (right).*

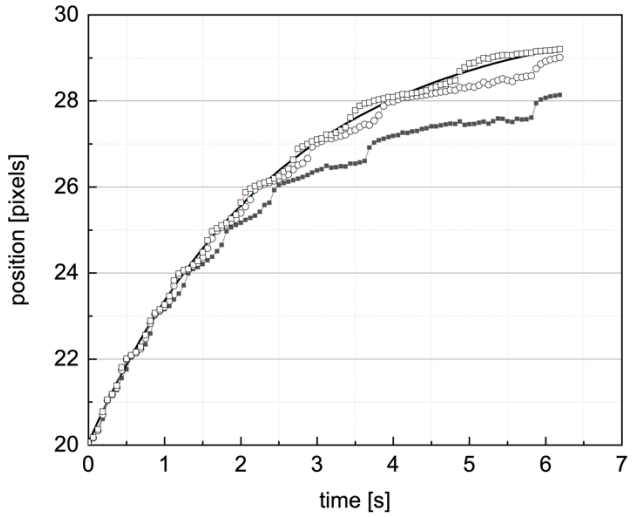

Fig. SI7: Test of the Tracker software (II): effect of the "evolve rate" parameter*. The plot compares the result of the tracking of the movement of a simulated microstructure with different values of the "evolve rate" parameter in the automatic Tracker software: 20% (solid squares), 10% (open circles) and 7% (open squares). The solid line represents the predicted displacement based on Eq. 4.1. The pixel size is 1 µm.*

5. Euler-Bernoulli theory applied to hollow microstructures

A prismatic beam with length L and uniform elastic modulus E under pure bending is bent into an arc that can be described by the displacement $x(z)$ with respect to the straight configuration as a function of the distance z of the cross-section from the constrained base of the beam. When the force only acts perpendicularly to the free section of the beam within the elastic regime, the curvature ρ of the neutral surface is given by:[3]

$$\frac{1}{\rho} = \frac{M}{EI} \tag{5.1}$$

Here M is the momentum of the applied force F (bending momentum) and I is the area momentum of inertia.[3] When the force F is applied only to the free tip of the beam (F_{tip}), $(z) = F_{tip}z$. Therefore, for small curvatures we can write the approximate differential equation:

$$\frac{d^2x}{dz^2} = \frac{M(z)}{EI} = \frac{F_{tip}z}{EI} \tag{5.2}$$

The product EI is constant, and the shape of the beam is found by integrating **Eq. 5.2**:

$$EI\frac{dx}{dz} = \int F_{tip}z\,dz = \frac{1}{2}F_{tip}z^2 + C_1 \tag{5.3}$$

In **Eq. 5.3**, C_1 is an integration constant that is determined by the boundary conditions (at the fixed end $z = L$, $\frac{dx}{dz} = 0$) as $C_1 = -\frac{1}{2}F_{tip}L^2$. By integration of **Eq. 5.3**, we obtain:

$$EIx(z) = \int\left(\frac{1}{2}F_{tip}z^2 - \frac{1}{2}F_{tip}L^2\right)dz = \frac{1}{6}F_{tip}z^3 - \frac{1}{2}F_{tip}L^2z + C_2 \tag{5.4}$$

The constant C_2 is determined by the boundary conditions (at the fixed end the deflection is zero: at $z = L$, $x = 0$). Hence, the equation of the elastic curve can be written as:

$$x(z) = \frac{F_{tip}}{6EI}\left(z^3 - 3L^2 z + 2L^3\right) \tag{5.5}$$

The total deflection at the free end of the beam is obtained by letting $z = 0$ in **Eq. 5.5**:

$$\delta x_{eq} = \frac{F_{tip} L^3}{3EI} = \frac{F_{tip}}{k_{eff}} \tag{5.6}$$

$k_{eff} = 3EI/L^3$ acts as en effective elastic bending constant.

In the case of a force which varies along the beam length, one defines the force per unit length through the relations $\frac{dM}{dz} = V(z)$ and $\frac{dV}{dz} = -f(z)$, and **Eq. 5.2** becomes:

$$\frac{d^4 x}{dz^4} = -\frac{f(z)}{EI} \tag{5.7}$$

For a constant force per unit length, $f = \frac{F}{L}$, and a constant product EI along the beam, the formal solution of **Eq. 5.7** can be found by consecutive integrations and by applying boundary conditions ($x(0) = 0; x'(0) = 0; M(L) = 0; V(L) = 0$). The resulting bending curve is:

$$x(z) = \frac{f}{24EI}\left(x^4 - 4Lx^3 + 6L^2 x^2\right) \tag{5.8}$$

We find that the total deflection of the beam at the free end is:

$$\delta x_{eq} = \frac{fL^4}{8EI} = \frac{FL^3}{8EI} = \frac{F}{k_{eff}} \tag{5.9}$$

with effective elastic constant $k_{eff} = 8EI/L^3$.

The area momentum of inertia I, needed for both **Eq. 5.6** and **Eq. 5.9**, can be computed by assuming a uniform composition of the pillars. For the circular and square cross-sections employed in the present work, the area momentum of inertia are:

$$I_{circular} = \frac{\pi}{4}(R^4 - r^4)$$

(5.10)

$$I_{square} = \frac{1}{12}(D^4 - d^4)$$

In **Eq. 5.10**, R and r are the external and internal radius of the circular cross-section and D and d are the external and internal side size of the square cross-section. As discussed in the main text, since the flow speed is rapidly decreasing in the 50-μm layer close to the glass wall of the capillary where the microstructures are fabricated, we assume that their bending is due only to the maximum force that acts on the microstructure tip, and derive the bending effective spring constant from **Eq. 5.6** as $k_{eff} = 3EI/L^3$.

6. Elastic constant of micro-helices

6.1 Equilibrium experiments

The elasticity of flexible microstructures can be studied by equilibrium and out of equilibrium experiments in solutions. In an experiment run at thermal equilibrium, a flexible structure immersed in a viscous medium at finite temperature undergoes thermal motion. By measuring the variance $\{\sigma_a^2\}_{a=x,y,z}$ of the position of a micro-structure tip, the equivalent spring constant $\{k_a\}_{a=x,y,z}$ can be estimated along each of the three coordinates, x, y and z (z is the symmetry axis) by the relation[4] $k_a = \frac{k_B T}{\sigma_a^2}$. Analogous approach is typically used also in the calibration of AFM tips[5,6].

We have tracked the tip of micro-helices by performing x-z time lapse experiments on a confocal laser-scanning microscope in transmission mode. The z axis lies along the cylindrical symmetry axis of the micro-structure. In order to measure accurately the variance of the a-th coordinate, we need a time resolution finer than the relaxation time τ of the damped elastic motions, that depends on the elastic constant and the viscous friction coefficient f as $\tau \cong k_a/f$. The condition on the time resolution is well satisfied in our experimental conditions (time resolution = 0.37 s) for the helicoidal microstructures endowed with small elastic constants, $k_a \simeq 0.003 - 0.04\ nN/\mu m$. Object tracking by transmission optical microscopy also provides a sufficiently high spatial resolution to resolve typical displacements of the order of 0.05 μm**.** An example of the observed fluctuations is given in **Fig. SI8A** for microhelices (sample H1 in **Table 1**, main text; length = 50 μm). The mean square

displacement of the z- coordinate of the helix tip is sensibly different from that of the transversal coordinates (x,y)**.** The distribution of the fluctuations around the average position can be described by a Gaussian function (**Fig. SI8B,C**) with variances $\sigma_{x,y}^2 = 1150\ nm^2$ and $\sigma_z^2 = 63\ nm^2$. The corresponding elastic constant values are $k_{x,y} \cong (3.50 \pm 0.04)\ pN/\mu m$ and $k_z \cong (64.2 \pm 0.7)\ pN/\mu m$: the first is due to bending motion perpendicularly to the helix axis and the second one is due to compression dynamics along the helix axis.

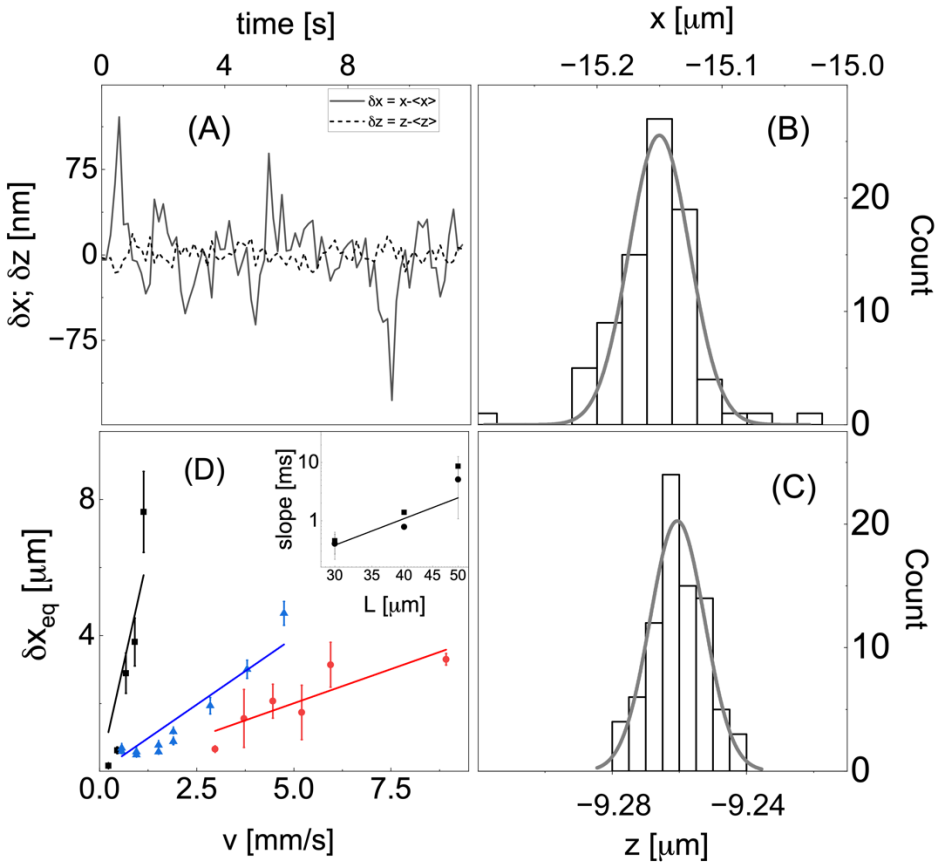

Fig. SI8: characterization of the elastic constant of micro-helices*. (A): Fluctuations of the position along the x and z axes of the tip of a micro-structured helix (diameter = 8* μm*, pitch = 6* μm*, length = 50* μm*) as a function of time at the equilibrium (no flow applied; the tip of the helix was tracked by means of the Tracker Video software). (B), (C): Histograms of the x and z fluctuations. The gray solid lines are Gaussian fits to the histograms with variances* $\sigma_{x,y}^2 = 1150\ nm^2$ *and* $\sigma_z^2 = 63\ nm^2$*, respectively. (D): maximum equilibrium deflection of helicoidal microstructures (samples H1, H2 and H3 in Table 1 of the main text, indicated by black squares, blue triangles and red circles, respectively) under constant flow with speed 0.5* $\leq v \leq$ *8 mm/s. Solid lines are linear fits to the data. Inset: log plot of the slope of* $\frac{d\delta x}{dv} \cong \frac{k}{v}$ *as a function of the helix length, L. The solid line is the fit to a power law* $\frac{d\delta x}{dv} = s\,L^p$ *with best fit values* $s = 6 \times 10^{-3} \frac{s}{m}$ *and* $p = 3.7$.

6.2 Out-of-equilibrium experiments

From a simple analysis of **Eq.4** in the main text, we expect that the effective elastic constant of the microstructures scales as $\approx L^{-3}$. Therefore, by decreasing the length of the micro-helices we should observe a rapid increase of the effective elastic constant that would prevent us from measuring it with an equilibrium approach as in **Fig. SI8A-C**. However, we can retrieve it from the measurement of the deflection δx_{eq} reached by the micro-helices under the action of a constant drag force (**Fig. SI8D** and **Fig. SI9**). To this purpose, micro-helices with the same pitch and diameter but decreasing length (**Table 1** in the main text) were fabricated in a top-to-bottom scanning mode on the inner wall of a square microcapillary and subjected to microfluidic flow (**Fig. SI9**). The flow speed v_x at the tip needed to deflect the micro-helices increases rapidly at decreasing helix length: the slope $\frac{d\delta x_{eq}}{dv} = f/k_{eff}$ should scale approximately as L^4, since the friction coefficient scales approximately as L and $k_{eff} \approx L^{-3}$. Even if it is approximated due to additional effects of the geometry of the micro-helices on the friction coefficient, the resulting scaling law, $\frac{d\delta x_{eq}}{dv} = L^4$, well describes the data collected for micro-helices with $30\ \mu m \leq L \leq 50 \mu m$ (**Fig. SI8D**). The best fit of the slope $\frac{d\delta x_{eq}}{dv}$ to the function of L^p (**Fig. SI8D**, inset) gives a slope p $\simeq 3.7$, in close agreement with the predicted fourth power. In order to measure the effective elastic constant from these out of equilibrium measurements, we should know the friction coefficient, f. Due to the particular geometry of the helixes, we can only approximate the friction coefficient to the one of a cylinder having the same diameter. Under this approximation, for the micro-helices listed in **Table 1** (main text), we can compute $f_{H1} \simeq 4.9 \times 10^{-8} \frac{Ns}{m}$, $f_{H2} \simeq 5.5 \times 10^{-8} \frac{Ns}{m}$ and $f_{H3} \simeq 6.2 \times 10^{-8} \frac{Ns}{m}$ and estimate the corresponding elastic constants as $k_{eff,H1} = (50 \pm 30)\ pN/\mu m$, $k_{eff,H2} = (70 \pm 30)\ pN/\mu m$, and $k_{eff,H3} = (140 \pm 10)\ pN/\mu m$.

Micro-helices are therefore endowed with particularly low bending elastic constants of the order of ~5-150 $pN/\mu m$.

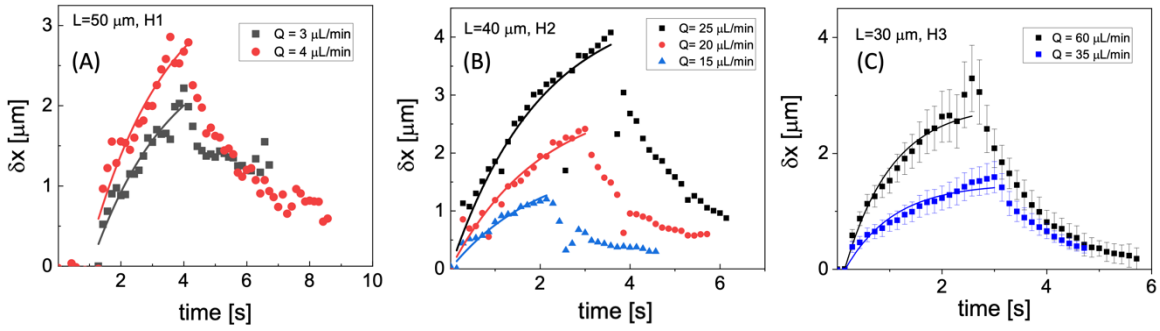

Fig. SI9. Bending dynamics of micro-helices under continuous flow *(volumetric flow rate* $3\mu L/\min \leq Q \leq 60\mu L/min$*.) (A) Temporal evolution of the deflection of a H1 micro-helix for* $Q = 3\ \mu L/min$ *and* $Q = 4\ \mu L/min$*. Solid lines are the best fit to an exponential growth with amplitude* $\delta x_{eq} = (3.3 \pm 0.2)\ \mu m$ *and growth time* $\tau = (0.9\ \pm 0.1)\ s$ *for* $Q = 3\ \mu L/min$*, and with* $\delta x_{eq} = (1.7 \pm 0.1)\ \mu m$ *and* $\tau = (0.9\ \pm 0.1)\ s$ *for* $Q = 4\ \mu L/min$*. (B): Temporal evolution of the deflection of a H2 micro-helix for* $Q = 25\ \mu L/min$*,* $Q = 20\ \mu L/min$ *and* $Q = 15\ \mu L/min$*. Solid lines are the best fit to an exponential growth with* $\delta x_{eq} = (4.6 \pm 0.4)\ \mu m$ *for* $Q = 25\ \mu L/min$*,* $\delta x_{eq} = (3.0 \pm 0.2)\ \mu m$ *for* $Q = 20\ \mu L/min$ *and* $\delta x_{eq} = (1.9 \pm 0.2)\ \mu m$ *for* $Q = 15\ \mu L/min$*. The growth time is* $\tau = (0.9\ \pm 0.1)\ s$ *for all the datasets. (C): Temporal evolution of the deflection of a H3 micro-helix for* $Q = 60\ \mu L/min$ *and Q=* $35\ \mu L/min$*. Solid lines are the best fit to an exponential growth with amplitude* $\delta x_{eq} = (3.3 \pm 0.2)\ \mu m$ *for* $Q = 60\ \mu L/min$ *and* $\delta x_{eq} = (1.7 \pm 0.1)\ \mu m$ *for* $Q = 35\ \mu L/min$*. The growth time is* $\tau = (0.9\ \pm 0.1)\ s$ *for both datasets.*

7. Analysis of the bending oscillatory dynamics

The bending dynamics of the stiff microstructures (i.e., structures with $k_{eff} \geq 10\ pN/\mu m$) is well described by the superposition of two exponential growth components $\delta x = A_1\left(1 - e^{-t/\tau_{fast}}\right) + A_2\left(1 - e^{-t/\tau_{slow}}\right)$, with average times $\tau_{fast} \leq 0.6\ s$ and widely variable $\tau_{slow} \cong 10 - 50\ s$. The fast component is under-resolved in our experimental setup. Examples of this type of bending dynamics measured under the action of a constant flow is given in the main text with **Fig.5B,D**.

For softer micropillars, we observe a clear and sustained oscillatory dynamics that cannot be ascribed to a pulsation in the flow actuated by the syringe pump in the micro-channel (see SI section 2). In order to characterize this behaviour, we have applied Fourier analysis to the AC component of the bending dynamics, $x_{AC}(t)$. This has been performed by selecting only the region in the dynamics where oscillations were visible, by fitting the trend to a fourth order polynomial, that simply describes the low frequency fluctuations $x_{LF}(t)$ in the position, and by applying the Fourier analysis to the difference $x_{AC}(t) = x(t) - x_{LF}(t)$. This procedure, outlined in **Fig. SI10**, allows us to

put into evidence the frequency components associated to the observed oscillatory behaviour, while taking apart the low frequency components of the whole Fourier spectrum.

In the following, we describe the workflow of the Fourier analysis in detail. At first, in the original data we select a stretch of time encompassing only the bending growth (**Fig. SI10A**). We define a time window (Δt) between a starting time and an ending time for the analysis (vertical lines in **Fig. SI10A**). The original data is low pass filtered and fit to a fourth-order polynomial function (**Fig. SI10B**) that we define as $x_{LF}(t)$. The AC component of the position is computed as $x_{AC}(t) = x(t) - x_{LF}(t)$ (**Fig. SI10C**). The FFT spectrum of this dataset is computed on windows of the same time length, Δt, sliding over the growing part of the bending dynamics. At least 4 windows are averaged (**Fig. SI10A**) to provide the average FFT spectrum that is then fit to a sum of Gaussian components, $\sum_i \frac{A_i}{\sigma_i\sqrt{\pi/2}} exp\left(-2\left(\frac{f-f_i}{\sigma_i}\right)^2\right)$. For each component, the maximum amplitude $m_i = \frac{A_i}{\sigma_i\sqrt{\pi/2}}$ is taken as a weight. The fractional weight of each component is then computed as $x_i = 100\frac{m_i}{\sum_i m_i}$.

We have computed two types of average values of the frequency that allow us to characterize the spectrum, referred to as $\langle f \rangle$ and $\langle f \rangle_{Th}$:

$$\langle f \rangle = \frac{\sum_i m_i f_i}{\sum_i m_i} = \frac{\langle f \rangle}{\sum_i m_i} = \frac{\langle f \rangle}{M} \tag{7.1}$$

$$\langle f \rangle_{Th} = \frac{\sum_i m_i f_i \Big|_{x_i > Th}}{\sum_i m_i \Big|_{x_i > Th}} \tag{7.2}$$

The second parameter, which is based on a threshold Th on the frequencies fractional weights, is particularly valuable when the spectrum is dominated by one or few components with similar

values of the frequency f_i. We adopted here a value of the threshold Th = 7%. In the example given in **Fig. SI10** and **Fig. SI11**, the best fit values of the Gaussian components needed to describe satisfactorily the spectrum is reported in **Table SI1**, leading to $\langle f \rangle$ = (2.5 $\pm$ 0.4) Hz and $\langle f \rangle_{Th}$ = (2.4 $\pm$ 0.3) Hz. The uncertainty on the two values is computed with the second order momentum $\langle f^2 \rangle = \sum_{i=1..M} \left(\frac{m_i}{M} f_i^2 \right)$, as $\sqrt{\langle f^2 \rangle - \langle f \rangle_{Th}^2}$. In the example given in **Table SI1**, the uncertainties are 0.4 Hz and 0.12 Hz for $\langle f \rangle$ and $\langle f \rangle_{Th}$, respectively.

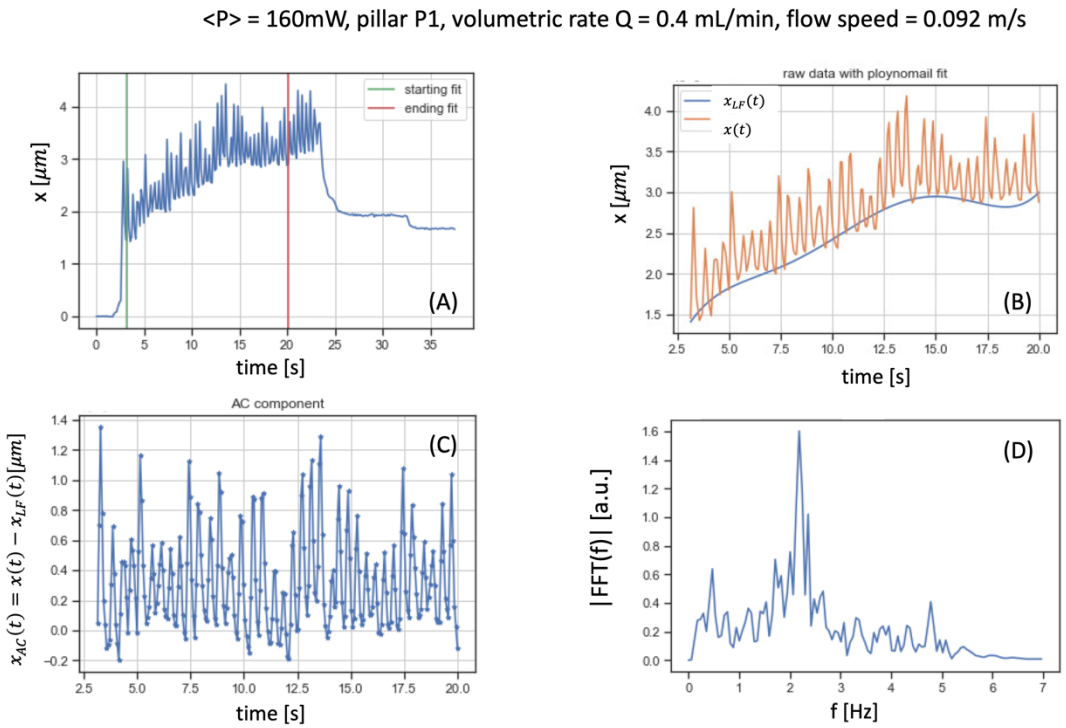

Fig. SI10: Workflow of the Fast Fourier transform analysis of the bending dynamics*. The example is given on a micropillar (sample P1 in Table 1 of the main text) fabricated at I=0.88 TW/cm², under a continuous volumetric flow rate Q=0.4 mL/min. (A): Raw displacement data,* $x(t)$, *with the markings (vertical lines) of the start and end point of the FFT analysis. (B): Superposition of the raw data (orange) with the low frequency component,* $x_{LF}(t)$ *(blue continuous line), obtained by a fourth power polynomial fit to the low pass filtered data. (C): AC component,* $x_{AC}(t) = x(t) - x_{LF}(t)$*. (D): FFT spectrum of the AC component.*

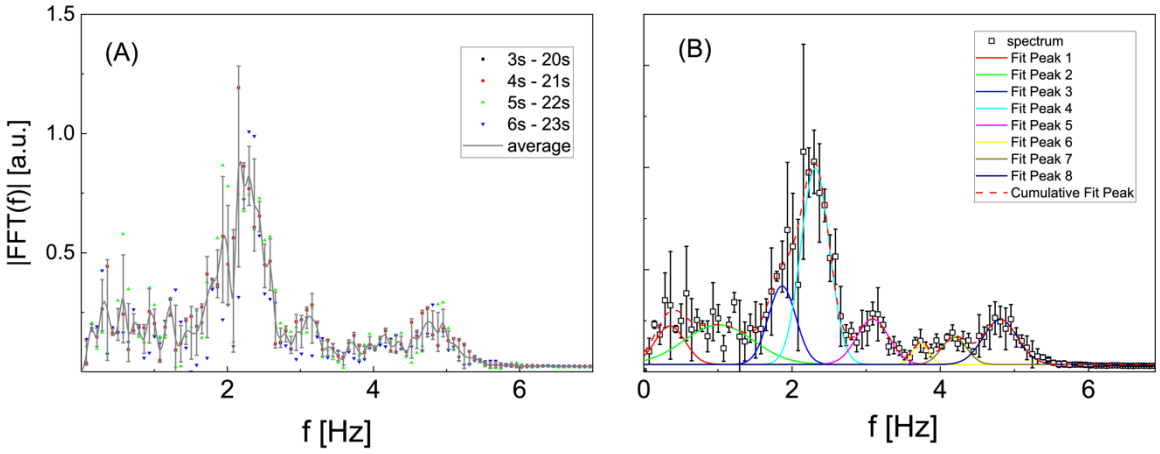

Fig. SI11: Fast Fourier analysis of the AC component of the structures bending. *(A): the FFT spectrum of* $x_{AC}(t)$ *is computed over an equal stretch of time (*$\Delta t = 17\ s$*) and averaged over at least 4 time windows (sliding window average). (B): the averaged FFT spectrum (open squares) is fit to a sum of 8 Gaussian components. The best fit overall spectrum is reported as red dashed line. The data refer to a micropillar fabricated at I = 0.88 TW/cm², under a flow speed* $v \simeq 0.09 \frac{m}{s}$ *at the structure tip.*

Table SI1. Best-fit parameters of the multi-Gaussian fit of the FFT spectrum of the bending dynamics.

n	1	2	3	4	5	6	7	8
f_i [Hz]	0.35	1.0	1.90	2.30	3.10	3.70	4.18	4.81
σ_i[Hz]	0.40	0.93	0.37	0.38	0.43	0.21	0.34	0.46
$A_i \times 10^6$	0.76	1.82	1.43	3.70	0.97	0.22	045	1.0
m_i	1.5	1.6	3.1	7.7	1.8	0.83	1.1	1.8
x_i	7.8	8.1	16.0	39.9	9.3	4.3	5.6	9.1
$m_i f_i$ [Hz]	0.54	1.6	5.7	18	5.5	3.1	4.5	8.5
$m_i f_i^2$ [Hz^2]	0.19	1.6	11	41	17	12	19	41

Table SI1. Result of the best fit of the average FFT spectrum reported in Fig. SI11B (dashed red line) to a sum of 8 Gaussian components of the type: $|\text{FFT}| = \frac{A_i}{\sigma_i\sqrt{\pi/2}} exp\left(-2\left(\frac{f-f_i}{\sigma_i}\right)^2\right)$. The amplitude of the components are $m_i = \frac{A_i}{\sigma_i\sqrt{\pi/2}}$. The fraction of each component is $x_i = 100\frac{m_i}{\sum_i m_i}$. The momenta are computed as $\langle f \rangle = \sum_i m_i f_i$ and $\langle f^2 \rangle = \sum_i m_i {f_i}^2$.

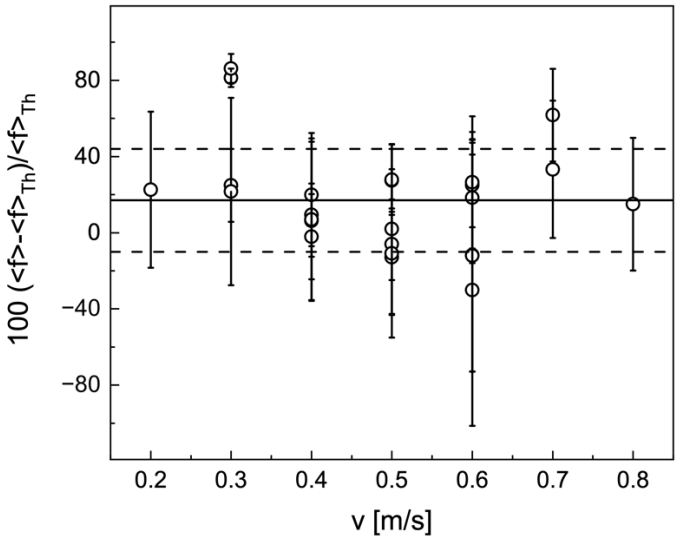

***Fig. SI12**. Evaluation of the difference between $\langle f \rangle$ (the average of the frequencies weighted over their amplitude) and $\langle f \rangle_{Th}$ (the average of the frequencies limited to the components with amplitude larger than a minimum threshold Th) as a function of the flow speed acting on the microstructures. For a threshold Th=7%, the difference between $\langle f \rangle$ and $\langle f \rangle_{Th}$ is limited on the average to 17% (solid line) with 25% standard deviation (dashed lines), supporting the idea that there is a dominant component in the bending spectra.*

8. Global fit of the frequency spectrum

We have searched for a possible universal description of $\langle f \rangle_{Th}$, and of the FFT amplitude FFT_{amp}, as a function of a rescaled variable $v_{resc} = v k_{eff}^{\alpha}$, that takes into account both the effect of the drag force (through the speed) and of the elastic force (through k_{eff}). It is noteworthy that for $\alpha = 0.5$, this parameter is proportional to the mechanical frequency $f_{mech} = \frac{1.9^2 D}{8\pi L^2}\sqrt{\frac{E}{\rho_p}} \approx \sqrt{\frac{k_{eff}}{m}}$ (D, L and ρ_p are the cross-section size, the height and the polymer density, respectively).

With the aim of finding the rescaling exponent α, we assumed a trial function to describe both the FFT_{amp} and the $\langle f \rangle_{Th}$ data. We assumed here that a fourth power polynomial ($poly(v_{resc}, P)$) can describe with reasonable accuracy the data trend (P is the 5 components parameter vector). We then built a global metric by summing the squared residuals of both the $\langle f \rangle_{Th}$ and the FFT_{amp} parameters with respect to the respective trial functions, over all the polymerizing conditions (laser intensity) and geometries (shapes) that give rise to oscillatory behaviour in the bending dynamics

(i.e. 0.8 nN/$\mu m \leq k_{eff} \leq$ 8 nN/μm). Chi-squares χ_f^2 and χ_a^2 are normalized to the value of the dependent variables as:

$$\chi_f^2 = \sum_i \frac{\left(\langle f \rangle_{Th} - poly4\left(v_{resc,i}, P_f\right)\right)^2}{\langle f \rangle_{Th,i}}$$

$$\chi_a^2 = \sum_i \frac{\left(FFT_{Amp,i} - poly4(v_{resc,i}, P_a)\right)^2}{FFT_{Amp,i}}$$

(8.1)

$$\chi_{tot}^2 = \chi_f^2 + \chi_a^2$$

The vectors P_f and P_a are the coefficients of the fourth order polynomials used to describe the trend of $\langle f \rangle_{Th}$ and the FFT_{amp}, respectively.

For each value of α, we minimized the global metric χ_{tot}^2 with respect to the parameters of the trial functions finding a best fit $\chi_{tot,bf}^2$. The plot of $\chi_{tot,bf}^2$ as a function of α, reported in **Fig. SI13**, indicates a very wide minimum around $\alpha \cong 0.35$ due to the combination of an increasing trend for χ_f^2 and a decreasing trend for χ_a^2. As it can be seen in **Fig. SI14B**, the best fit $\alpha \cong \frac{1}{3}$ would correspond to a hyperbolic decrease $FFT_{amp} \cong v_{resc}^{-2}$. The universal trend becomes even clearer for larger values of α (**Fig. SI14C**). However, we could not recover any clear universal trend of $\langle f \rangle_{Th}$ as function of v_{resc} for α > 0.4. These considerations are the origin of the (wide) minimum observed for $\chi_{tot,bf}^2$ as a function of α (**Fig. SI13**). The large width of the minimum in **Fig. SI13** is also clearly due to our initial wrong assumption on the shape of a universal description of the frequency $\langle f \rangle_{Th}$ as a function of v_{resc}. Indeed, from **Fig. SI14D,E**, we can point out that the average oscillation frequency $\langle f \rangle_{Th}$ has a discrete jump at about $v_{resc} \cong 0.015 \frac{m}{s}\left(\frac{N}{m}\right)^{0.35}$, and below and above this threshold the trend of $\langle f \rangle_{Th}$ can be described by simple linear (or at most quadratic) trends (dashed lines in **Fig. SI14E**).

Overall, these considerations led us to consider α = 0.35 as the best value of the exponent for which a single universal behaviour can be observed in the bending dynamics of flexible microstructures. Such a universal trend of the values of both $\langle f \rangle_{Th}$ and FFT_{amp} as a function of the rescaled speed $v_{resc} = vk_{eff}^{\alpha}$ for α = 0.35 is reported in **Fig. SI15**, along with the comparison of the results obtained for $\alpha = 0.5$. It is clear that a double regime better describes the measured trend of the oscillation frequencies. Due to the uncertainty on FFT_{amp}, it is not possible to bring into evidence a similar double behaviour in the corresponding plot.

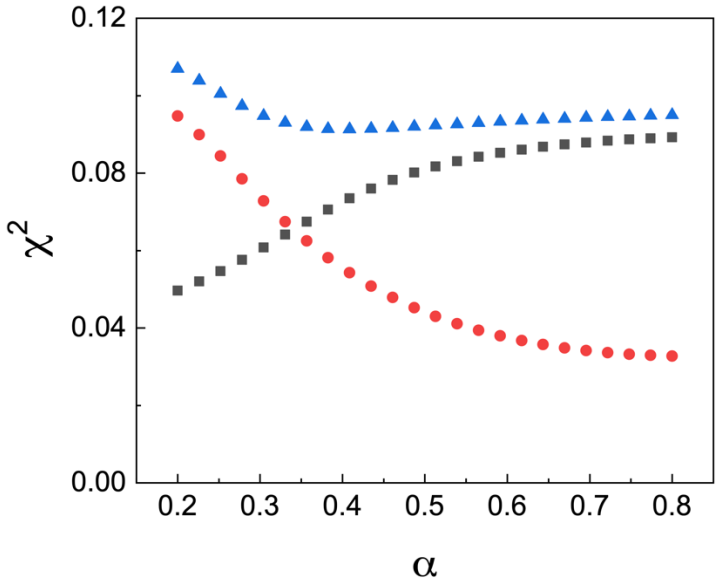

Fig. SI13: Dependence of the best-fit chi-square value as a function of the scale exponent α. *The values of* $\chi^2_{f,bf}$, $\chi^2_{a,bf}$ *and* $\chi^2_{tot,bf}$ *(Eq. 8.1) correspond to squares, circles and triangles, respectively. The chi-square values are the best-fit values obtained by fitting to a fourth order polynomial the trend of* $\langle f \rangle_{Th}$ *and* FFT_{amp} *as a function of* $v_{resc} = vk_{eff}^{\alpha}$.

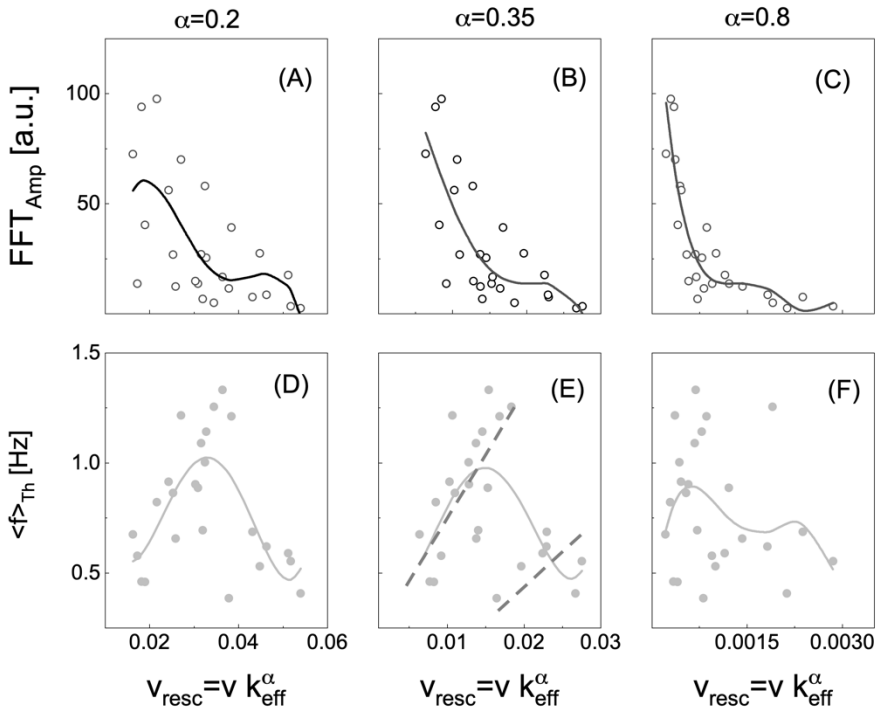

Fig. SI14: Dependence of $\langle f \rangle_{Th}$ ***and of*** FFT_{amp} ***on the rescaled speed*** v_{resc} ***as a function of the scale exponent*** α*. (A)-(F): Best fit of the trend of* FFT_{amp} *(open circles, panels A-C) and of* $\langle f \rangle_{Th}$ *(filled circles, panels D-F) as a function of* $v_{resc} = vk_{eff}^{\alpha}$ *to a fourth-order polynomial for three values of* $\alpha = 0.2, 0.35$ *and* 0.8*. The solid lines are the best fit functions* $poly4(v_{resc}, P_{f,bf})$ *and* $poly4(v_{resc}, P_{a,bf})$*, where* $P_{f,bf}$ *and* $P_{a,bf}$ *are the best fit parameter vectors. The dashed lines in (E) are the best linear fits to* $\langle f \rangle_{Th}$ *as a function of* $v_{resc} = vk_{eff}^{\alpha}$ *below and above the threshold point* $v_{resc} \cong 0.015 \frac{m}{s}\left(\frac{N}{m}\right)^{0.35}$.

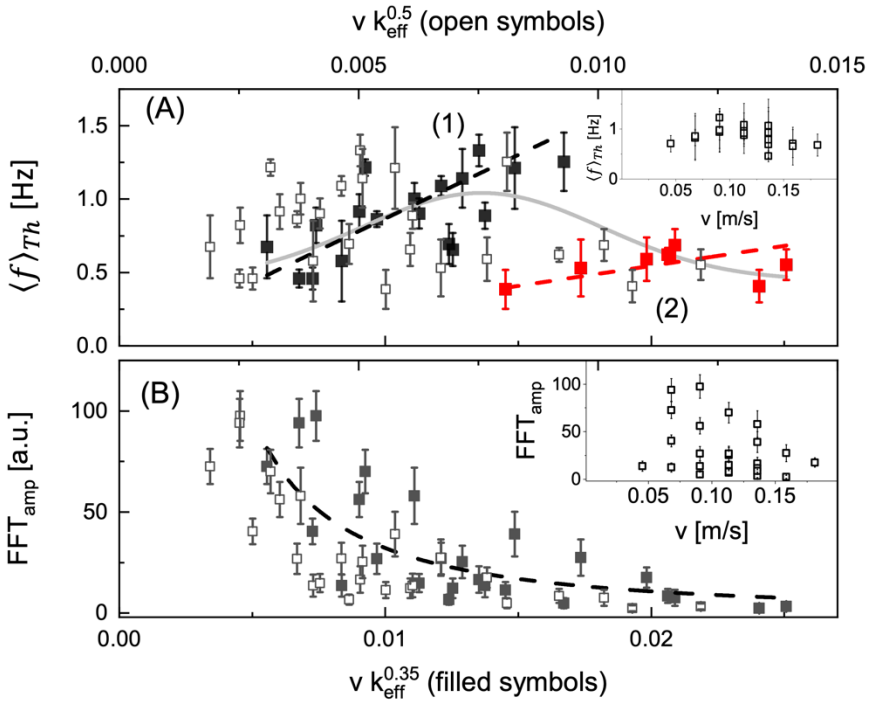

Fig. SI15: Results of the Fourier analysis of the oscillatory bending dynamics for microstructures with square and circular cross-sections. *(A): Fourier frequency* $\langle f \rangle_{Th}$*, evaluated as an average of the most abundant frequencies of the FFT spectra weighted over the corresponding amplitudes.* $\langle f \rangle_{Th}$ *is plotted as a function of the rescaled flow speed* $v_{resc} = vk_{eff}^{\alpha}$*, for* $\alpha = 0.35$ *(lower scale, filled symbols) and* $\alpha = 0.5$ *(upper scale, open symbols). The grey line is a Gaussian fit to the data (* $\alpha = 0.35$ *only) to guide the eye. The two dashed lines are best linear fit to the frequency data below (black symbols) and above (red symbols) the threshold* $vk_{eff}^{0.35} = 0.015\,\frac{m}{s}\left(\frac{N}{m}\right)^{0.35}$*. Inset:* $\langle f \rangle_{Th}$ *as a function of the flow speed at the tip of the structure (*$\alpha = 0$*). (B): FFT amplitudes for the same cases of panel (A). The dashed line is the best hyperbolic fit* $FFT_{amp} \cong v_{resc}^{-2}$ $(\alpha = 0.35)$*. Inset:* FFT_{AMP} *as a function of the flow speed (*$\alpha = 0$*).*

9. Langevin equation for a non-linear spring

The full dynamic equation of a beam having cross-section C(z) and mass density ρ_p, fixed at one end and bending under the action of a force, is given by:[7]

$$EI\frac{\partial^4 x(z,t)}{\partial z^4} + \rho_p C(z)\frac{\partial^2 x(z,t)}{\partial t^2} + f\frac{\partial x(z,t)}{\partial t} = F(z,t) \qquad (9.1)$$

The first term is the elastic force due to the bending, the second term corresponds to the inertial term, the third one is the friction force simply due to viscosity. The right hand side of the equation represents the Brownian random force per unit length. We want to include in **Eq. 9.1** corrections due to the time dependence of the friction factor and viscoelasticity.

For the sake of simplicity we analyze the effect of a time dependent Young's modulus on the dynamics of a single mass constrained to a fixed point under the action of a constant drag force due to a flow field $\vec{v}(x,y,z)$ in a thermal bath. In the absence of obstacles and large turbulence in the capillary, the flow field has components only along the capillary axis (here the x-axis) and depends only on the transversal coordinates y and z. If there are obstacles along the flow, at Reynolds numbers $Re_y \geq 100$, there might be the onset of vortex shedding past the obstacle[8] with a characteristic frequency $f_s = \frac{v_{max}}{w} S_t$, where v_{max}, w and S_t are the maximum speed along the capillary axis, the width of the capillary and the Strouhal number that lies typically in the range $0.2 \leq S_t \leq 0.4$.[9,10] Therefore the velocity field will be approximated by a constant component $v_{xo}(z)$ plus a time varying component $\vec{\delta v}(x,y,z,t)$ whose spectrum has characteristic frequencies close to f_s. In the first approximation, when disregarding the presence of vortices, we can redefine the x coordinate with respect to the equilibrium bending value given by $x_{eq} = f v_{xo}/k_{eff}$ and write the equation of motion for the displacement along a direction perpendicular to the axis of symmetry as:

$$\frac{d^2x}{dt^2} = -\omega_0^2 x - \delta_x x - \gamma\frac{dx}{dt} + J \qquad (9.2a)$$

$$\frac{d^2x}{dt^2} = -\omega_0^2 x - \delta_x \otimes x - \gamma\frac{dx}{dt} + J \qquad (9.2b)$$

depending on whether a non-linear elasticity (stress-stiffening, **Eq.9.2a**) or a pure viscoelastic term (**Eq.9.2b**) are taken into account.[11] In this equation, $\omega_0^2 = \frac{k}{m}$ and $\gamma = f/m$, where f and m are the friction coefficient and the mass of the particle. In our case, $k \cong 6\frac{nN}{\mu m}$, $f \cong 6 \times 10^{-8}\frac{Ns}{m}$ and the mass of the microstructures is $m \cong 3\ ng$. Therefore, we can compute $\omega_0 \cong 28\ kHz$ and $\cong 20\ kHz$.

The viscoelastic term δ_x can be described by means of its Fourier spectrum[12] $\hat{\delta}_x(\omega) = \omega_\theta^2 \frac{(\theta - i\omega)\omega}{\omega^2 + \theta^2}$. Such a spectral dependence corresponds to an exponential response to an impulsive stress. A similar spectral dependence can be assumed for the case of stress-stiffening since the stress should follow the time dependence of the friction coefficient that follows that of the bending deformation. This one, in turn, is experimentally described by an exponential growth. J is the thermal (Gaussian) force defined by the first two momenta[4] $< I > = 0$; $< I(t)I(0) > = \frac{2K_B T f}{m^2}\delta(t)$, or by its flat Fourier spectrum with value $< |\hat{I}(\omega)|^2 > = \frac{2K_B T f}{m^2}$.

We are going to find an approximated solution to the deformation/displacement of a viscoelastic structure as a first order expansion with respect to the solution of the deformation dynamics of a pure elastic (non-viscoelastic) structure.

In the non-viscoelastic case ($\delta_x = 0$), it is well known that the time correlation function of the position of a particle subject to an elastic force with elastic constant k in a thermal bath is given by:[13]

$$C_{xx}(\tau) = \frac{K_B T}{k} e^{-\gamma t/2}\left(cos(\sqrt{\Delta}t) + \frac{\gamma}{2\sqrt{\Delta}} sin(\sqrt{\Delta}t)\right) \qquad (9.3)$$

In **Eq. 9.3,** $\Delta = \omega_0^2 - \frac{\gamma^2}{4}$, with $\omega_0^2 = \frac{k}{m}$. The system can be overdamped, when $\omega_0 < \frac{\gamma}{2}$, or critically damped, when $\omega_0 = \frac{\gamma}{2}$, and in this case the correlation function has no oscillatory behaviour. Alternatively, when $\omega_0 > \frac{\gamma}{2}$, the system is underdamped and the correlation function displays

oscillations with a period $T = \frac{2\pi}{\sqrt{\omega_0^2 - \frac{\gamma^2}{4}}}$. This result can be obtained by Fourier transforming **Eq. 9.2**[13] with $\delta_x = 0$:

$$\begin{cases} \hat{x}_0(\omega) = -\dfrac{\hat{J}}{(\omega - \omega_+)(\omega - \omega_-)} = -\dfrac{\hat{J}}{G_F(\omega)} \\ G_F(\omega) = (\omega - \omega_+)(\omega - \omega_-) \\ \omega_\pm = -i\dfrac{\gamma}{2} \pm \sqrt{\Delta} \end{cases} \qquad (9.4)$$

This is the spectrum of the bending dynamics of the pure elastic case. The position correlation function in the Fourier space is given by the square modulus of **Eq.9.4**:

$$\hat{C}_{xx}(\omega) = \frac{\langle |\hat{J}|^2 \rangle}{|\omega - \omega_+|^2 |\omega - \omega_-|^2} \qquad (9.5)$$

The poles of this spectrum are $\omega_{1,2} = -i\frac{\gamma}{2} \pm \sqrt{\Delta}$ and $\omega_{3,4} = i\frac{\gamma}{2} \pm \sqrt{\Delta}$. Due to our definition of the Fourier transform, $\hat{y}(t) = \frac{1}{2\pi}\int y(\omega) e^{-i\omega t} d\omega$, we can accept only the poles $\omega_{1,2}$ with negative imaginary component (to ensure that the Fourier kernel vanishes for $|\omega| \to \infty$) and the solution is **Eq. 9.3**. The presence of a damping term $\approx e^{-\gamma t/2}$ in the correlation function means that the fluctuations in the underdamped conditions are vanishing exponentially with relaxation time $\cong \frac{2}{\gamma} \simeq 160\ \mu s$.

Non-linear elastic spring.

We now treat the two cases of non-linear elastic response, described by **Eq.9.2a**, and of pure visco-elastic response, described by **Eq.9.2b**, separately. In the non-linear elasticity case, the mechanical response depends also on the product of the deformation, x(t), times the non-linear part of the modulus, $\delta_x(t)$, translating in the Fourier space in the convolution of the function $\hat{\delta}_x(\omega)$ with the bending deformation spectrum, $\hat{x}(\omega)$. In the pure viscoelastic case, the mechanical response depends also on the convolution of the viscoelastic response with the deformation translating in

the Fourier space in the product of the function $\delta_x(\omega)$ with the bending deformation spectrum, $\hat{x}(\omega)$.

Stress-stiffening dynamics of a spring. When taking into account the non-linear term $\approx \delta_x x$ in **Eq. 9.2a** the dynamics is described in the Fourier space by:

$$G_F(\omega)\hat{x}(\omega) = -\hat{J} + \left(\hat{\delta}_x \otimes \hat{x}\right)(\omega) \tag{9.6}$$

An approximate solution of the viscoelastic dynamics (**Eq. 9.6**) can be obtained by substituting to $\hat{x}(\omega)$ the elastic solution $\hat{x}_0(\omega) = -\hat{J}/G_F(\omega)$ in the convolution term of **Eq. 9.6**:

$$G_F(\omega)\hat{x}(\omega) \simeq -\hat{J} - \left(\hat{\delta}_x \otimes \frac{\hat{J}}{G_F(\omega)}\right)(\omega) \tag{9.7}$$

We first compute the convolution term of **Eq. 9.7**:

$$\left(\hat{\delta}_x \otimes \frac{\hat{J}}{G_F(\omega)}\right)(\omega) = \omega_\theta^2 \int ds \frac{(\omega - s)}{(\theta + i(\omega - s))} \frac{\hat{J}}{G_F(s)} \tag{9.8}$$

We consider again the poles of the kernel with negative imaginary part, $\omega = s - i\theta$ and $\omega = \omega_{\pm} = -i\frac{\gamma}{2} \pm \sqrt{\Delta}$. The solution is then:

$$\left(\hat{\delta}_x \otimes \frac{\hat{J}}{G_F(\omega)}\right)(\omega) = -i\omega_\theta^2 \hat{J} \left[\frac{+i\theta}{[\omega - i\theta - \omega_+][\omega - i\theta - \omega_-]} + \frac{(\omega - \omega_+)(\omega - \omega_+ + i\theta)}{2\sqrt{\Delta}\left[\theta^2 + (\omega - \omega_+)^2\right]} - \frac{(\omega - \omega_-)(\omega - \omega_-}{2\sqrt{\Delta}\left[\theta^2 + (\omega - \right.} \right. \tag{9.9}$$

The second and third term can be combined to give:

$$\left(\hat{\delta}_x \otimes \frac{\hat{J}}{G_F(\omega)}\right)(\omega) =$$

(9.10)

$$= \omega_\theta^2 \hat{J}\,\theta\left\{\frac{1}{G_F(\omega - i\theta)} + \frac{G_F(\omega)}{G_\delta(\omega)} - \theta\frac{2i\omega + (\theta+\gamma)}{G_\delta(\omega)}\right\}$$

Where $G_\delta(\omega) = \left[\theta^2 + (\omega - \omega_+)^2\right]\left[\theta^2 + (\omega - \omega_-)^2\right]$. By substituting **Eq. 9.10** into **Eq. 9.6** we can write the first order approximation of the spectrum, $\hat{x}(\omega)$:

$$\hat{x}(\omega) = -\frac{\hat{J}}{G_F(\omega)} - \frac{\hat{J}\omega_\theta^2}{G_F(\omega)}\theta\left\{\frac{1}{G_F(\omega - i\theta)} + \frac{G_F(\omega)}{G_\delta(\omega)} - \theta\frac{2i\omega + (\theta+\gamma)}{G_\delta(\omega)}\right\} =$$

(9.11)

$$= -\frac{\hat{J}}{G_F(\omega)} - \theta\omega_\theta^2\frac{\hat{J}}{G_F(\omega)G_F(\omega - i\theta)} - \omega_\theta^2\theta\frac{\hat{J}}{G_\delta(\omega)} + \theta^2\hat{J}\omega_\theta^2\frac{2i\omega + (\theta+\gamma)}{G_\delta(\omega)G_F(\omega)}$$

The poles of **Eq. 9.11** are those of the functions $G_F(\omega)$, $G_F(\omega - i\theta)$ and $G_\delta(\omega)$. However, the behavior of the four right hand terms of **Eq. 9.11** differs in a few points:

- The first term has poles $\omega_\pm = -i\frac{\gamma}{2} \pm \sqrt{\Delta}$ and contains therefore an exponential term $\cong e^{-\gamma t/2}$ superimposed to an oscillation with period $T = 2\pi/\sqrt{\Delta}$.
- The second term has two additional poles, $\omega'_\pm = -i\left(\frac{\gamma}{2} - \theta\right) \pm \sqrt{\Delta}$.
- The third term has only the poles given by $G_\delta(\omega) = 0$, that are again $\omega'_\pm = -i\left(\frac{\gamma}{2} - \theta\right) \pm \sqrt{\Delta}$. These, in the case when $\frac{\gamma}{2} \geq \theta$, correspond to a damped oscillation with the same period. The characteristic decay time of the position autocorrelation function is then $\cong 1/\left(\frac{\gamma}{2} - \theta\right) > 2/\gamma$. Possibly, when $\theta \to \frac{\gamma}{2}$ we can reach the situation of a pure (undamped) oscillatory motion or a very slow decay.
- The fourth term has both the poles $\omega_\pm$ and $\omega'_\pm$.

As a result of this analysis, we conclude that there is the possibility to have sustained (i.e. undamped) oscillatory behaviour in the bending of the microstructures whenever $\Delta = \omega_0^2 - \frac{\gamma^2}{4} > 0$, if there exists a relaxation mode in the Young's modulus with rate $\theta \rightarrow \frac{\gamma}{2}$.

In the present case, for the microstructures exhibiting the sustained oscillations, the mass is $m \cong 3\ ng$ and the effective elastic constant is $k_{eff} \cong 6\ nN/\mu m$: the typical value of the resonance angular frequency is $\omega_0 \cong 1.3\ kHz$. As previously noted, at low Reynolds number the friction coefficient for a straight micro-pillar is of the order of $f \cong 6 \times 10^{-8} \frac{Ns}{m}$, that corresponds to a damping frequency $\gamma \cong 20\ kHz$. We can therefore have oscillations of the structure, though with a high angular frequency $\sqrt{\Delta} \cong 1.3\ kHz$, two orders of magnitude larger that the angular frequencies observed here $\cong 2\ \pi\ 1.5\ Hz = 10\ Hz$.

However, there are additional sources of non-linearity: for example, the change in the friction coefficient of the microstructures as they bend under the effect of the steady flow or the onset of turbulence. In these cases, the coupling of this additional sources of non-linearity with the one arising from the viscoelastic behavior, can lead to beatings at low frequencies and oscillatory behaviors similar to those observed in the present work.

The dependence of the friction coefficient on the bending, would imply that also the term $\gamma \frac{dx}{dt}$ becomes non-linear and brings into the Fourier analysis an additional convolution term with oscillatory components at frequencies of the order of $\sqrt{\Delta}$, similar to the undamped ones arising from viscoelasticity, that could beat with each other.

The situation is even clearer in the case of the onset of vortices at Reynolds numbers $Re_y = 40 - 200$, that is accompanied by oscillatory components in the flow past the bent microstructures and in the pressure field downstream of them. This implies the presence of a tiny oscillatory component in the drag force: this couples to the one of the friction factor in an additional term, acting as an external oscillatory force intrinsically coupled with the dynamics of the structure through the time dependence of the friction factor. We should then add to **Eq. 9.2** a term of the type $\gamma(y,t)\vec{\delta v}(x,y,t)$, where the characteristic frequency of the vortex term is $f_s = \frac{v_{max}}{w}\ S_t \cong 60Hz - 200Hz$ for our experimental conditions, and where the characteristic frequency of the

friction term $\gamma(y,t)$ is the one of the bending dynamics, or $\cong\frac{\sqrt{\Delta}}{2\pi}\cong 200Hz$, very close to the vortex frequency f_s. The beating of these two terms could then give rise to the observed low frequency sustained oscillations.

Pure viscoelastic spring.

In this case, the system is described by **Eq. 9.2b** and the dynamics in the Fourier space is described by:

$$G_F(\omega)\hat{x}(\omega) = -\hat{J} + \hat{\delta}_x(\omega)\hat{x}(\omega) \qquad (9.12)$$

We assume again that the Fourier spectrum in **Eq. 9.12** is given by $\hat{\delta}_x(\omega) = \omega_\theta^2\frac{\omega}{(\theta + i\omega)}$, as this is the description in the Fourier space of an exponential growth with growth time $\tau = \frac{1}{\theta}$, as observed experimentally.

The equation of the poles derived from **Eq.9.12** is:

$$G_F(\omega) - \hat{\delta}_x(\omega) = (\omega - \omega_+)(\omega - \omega_-) - \omega_\theta^2\frac{\omega}{(\theta + i\omega)} = 0 \qquad (9.13)$$

We can search for poles of the spectrum $\hat{x}(\omega)$ by setting $\omega = \omega_\pm + \epsilon$. With this change of variables, **Eq.9.13** becomes:

$$\epsilon(2\sqrt{\Delta} + \epsilon) - \frac{\omega_\theta^2(\epsilon + \omega_+)}{(\epsilon + \omega_+ + i\theta)} = 0 \qquad (9.14)$$

If we assume that the correction $\epsilon \ll \omega_0$ and $\omega_0 \gg \gamma$ (implying that $\sqrt{\Delta} \simeq \omega_0$), then we can approximate the solution of the third order **Eq. 9.14** with the following second order equation:

$$\begin{cases} \epsilon^2 + b\epsilon + c = 0 \\ b = 2\sqrt{\Delta} - \dfrac{i\theta\omega_\theta^2}{(\omega_\pm + i\theta)^2} \simeq 2\omega_0 - i\theta\dfrac{\omega_\theta^2}{\omega_0^2} \\ c = -\dfrac{\omega_\theta^2\omega_\pm}{\omega_\pm + i\theta} \simeq -\omega_\theta^2\left(1 \mp \dfrac{i\theta}{\omega_0}\right) \end{cases} \quad (9.15)$$

The solution of **Eq.9.14** that we search is then:

$$\epsilon = -\frac{b}{2} \pm \sqrt{\frac{b^2}{4} - c} \simeq -\frac{c}{b} \simeq \frac{\omega_\theta^2\left(1 \mp \dfrac{i\theta}{\omega_0}\right)}{\left(\pm 2\omega_0 - i\theta\dfrac{\omega_\theta^2}{\omega_0^2}\right)} \simeq \pm\frac{\omega_\theta^2}{2\omega_0} - i\theta\frac{\omega_\theta^2}{4\omega_0^2} \quad (9.16)$$

Therefore, the poles of the dynamic equation, **Eq. 9.12**, are approximated by:

$$\omega_\pm \simeq \pm\omega_0\left(1 + \frac{\omega_\theta^2}{2\omega_0^2}\right) - i\left(\frac{\gamma}{2} + \frac{\theta\omega_\theta^2}{4\omega_0^2}\right) \quad (9.17)$$

From **Eq. 9.17**, we can see that the oscillatory radial frequency is slightly increased due to the non-linearity of the spring. In addition, we point out that there is no possibility to overcome the damping rate γ by a correction factor due to the non-linearity of the spring, since the first order correction to this, $\dfrac{\theta\omega_\theta^2}{4\omega_0^2}$, is always positive.

10. The total fluid force acting on a sphere in intermediate Reynolds number regime.

The inertial force F_ρ, due to the fluid mass displacement, depends on the fluid density and it is quadratic with the object-flow speed for rigid objects[14]: $F_\rho = \dfrac{C_D}{2}\rho_{fl}A_x v^2$, where ρ_{fl} is the fluid (water) density, and $A_x \cong LD$ is the microstructure cross-section against the fluid. We approximate the flow speed along the x axis v with its value at the structure tip. The drag coefficient C_D can be obtained from studies of the flow past cylinders[8,15] and at low Reynolds number lies in the range

$0.9 \leq C_D \leq 1.1$. This expression is valid for high Reynolds number values, $Re_y \simeq 1000$ and above. At small values of the Reynolds number, $Re_y \simeq 1$ or below, we are in the creeping flow regime, where the fluid drag force on the object, assumed here as a sphere, can be written as $F_\eta = 6\pi\eta\frac{D}{2}v$.

In this work we explore an intermediate regime of Reynolds numbers and we have assumed that the overall force F_{tip} acting on the structure tip is given by $F_{tip} = F_\eta + F_\rho = fv + \frac{C_D}{2}\rho_{fl}A_x v^2$. As pointed out in the review process, this assumption cannot be taken for granted simply on the basis of the dimensional analysis of the Navier-Stokes equation (Eq. 2.38 in ref.[16]). The total drag force due to the fluid for a generic value of the Reynolds number is not the sum of the viscous and the inertial limits of the drag forces. However, the linear superposition of these two limiting cases can be used for a reasonable approximation of the total drag force. This assumption can be justified in analogy to the expansion[17] of the drag force over the Reynolds number, valid for $Re_y \leq 1$, and on the basis of experimental data[18] as detailed below.

In a narrow Reynolds number range, $Re_y \leq 1$, the drag force acting on a sphere of radius r in a viscous fluid of viscosity η and density ρ_{fl} is given by[17]:

$$F_{drag} \simeq 6\pi\eta v r\left[1 + \frac{3}{16}Re_y + \frac{9}{160}Re_y^2\left(\ln\left(\frac{Re_y}{2}\right) + \gamma'\right) + \frac{27}{640}Re_y^3 ln\left(\frac{Re_y}{2}\right) + O(Re_y^3)\right] \quad (10.1)$$

where $\gamma' = 0.5772 + \frac{5}{3}\ln(2) - \frac{323}{360}$.

At the first order in the Reynolds number this expression is a linear combination of the creeping flow and the turbulent flow limits, since the second term in this equation is $(6\pi\eta v r)\frac{3}{16}Re_y \propto F_\eta Re_y = \frac{18}{16}\pi r^2\rho v^2 \propto F_\rho$. If we compare Eq. (10.1) with the weighted sum of the creeping and turbulent limits, $F_\eta + C_D F_\rho$, where the turbulent term is weighed by the factor C_D, we find a very good agreement for $C_D \simeq 0.7$. The average square root mean error amounts to 1.8% over the range $0.0016 \leq Re_y \leq 1$ (see **Fig.SI16**). From this analysis we reason that a linear superposition of the two limiting expressions of the drag force F_η and F_ρ can describe reasonably

well the total drag force over a certain range of Reynolds numbers, even though this cannot be exactly derived from the analysis of the NS equations.

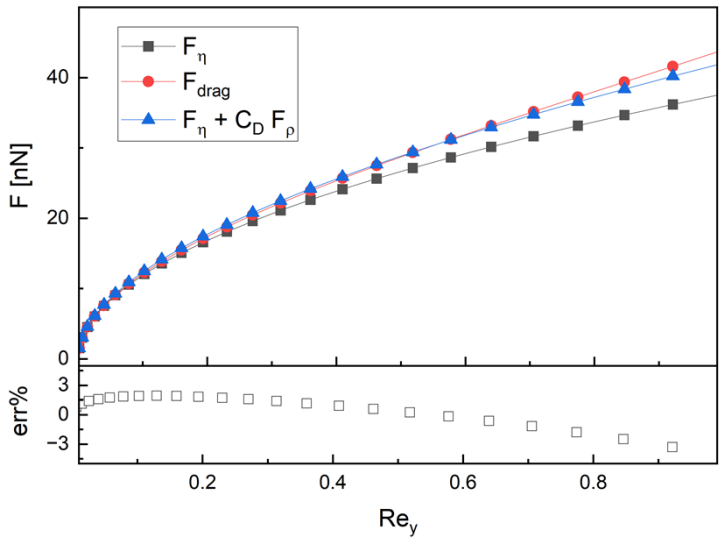

Fig. SI16: *Comparison of the total drag force acting on a sphere according to the approximation given in Eq.10.1 (Eq.4.2-21 from ref.[18], Proudman et al.[17]).* The approximation $F_\eta + C_D F_\rho$, is computed for $C_D = 0.7$. The bottom panel report the percentage error between Eq.10.1 and the approximated value $F_\eta + 0.7 F_\rho$.

In a much wider Reynolds number range, the description of the transition between the creeping to the turbolent regime of an object under the action of a total fluid force F_{tot} can be performed by defining an effective friction factor[18], $f_{app} = \frac{F_{tot}}{0.5\,\rho_{fl} A_x v^2}$. The trends of f_{app} on the Reynolds number are known for various geometries as reported for example in ref.[19] (Fig.6.52). For a sphere of radius $\frac{D}{2}$, approximating the tip of the structures investigated here (D is the diameter of the structure), one finds (see Ch.6 in ref.[18]) that $f_{app} \simeq \frac{24}{Re_y}$ for low values of $Re_y \leq 1$ and $f_{app} \simeq 0.44$ for $Re_y > 1000$. These two regimes correspond to the viscous force , $F_{tot} \simeq 6\pi\eta\frac{D}{2}v$, and to the inertial force, $F_{tot} \simeq \frac{C_D}{2}\rho_{fl}\pi\left(\frac{D}{2}\right)^2 v^2$. In the whole range the friction factor f_{app} is well approximated (Fig.6.3-1 in ref.[18]) by $f_{app} \simeq \left(\sqrt{\frac{24}{Re_y}} + 0.5407\right)^2$. We notice that for a sphere $C_D \simeq 0.44$ and for a cylinder $C_D \simeq 0.9$.

In the range $5 \leq Re_y \leq 150$ the discrepancy between the description $F_{tip} = \left(\sqrt{\frac{24}{Re_y}} + 0.5407\right)^2 \frac{\rho_{fl}}{2} \pi \left(\frac{D}{2}\right)^2 v^2$ and the form $F_{tip} = F_\eta + F_\rho = fv + \frac{C_D}{2} \rho_{fl} A_x v^2$, with the assumption $C_D = 0.9$, amounts to $\pm 14\%$ (**Fig. SI16**) in the range $5 \leq Re_y \leq 150$.

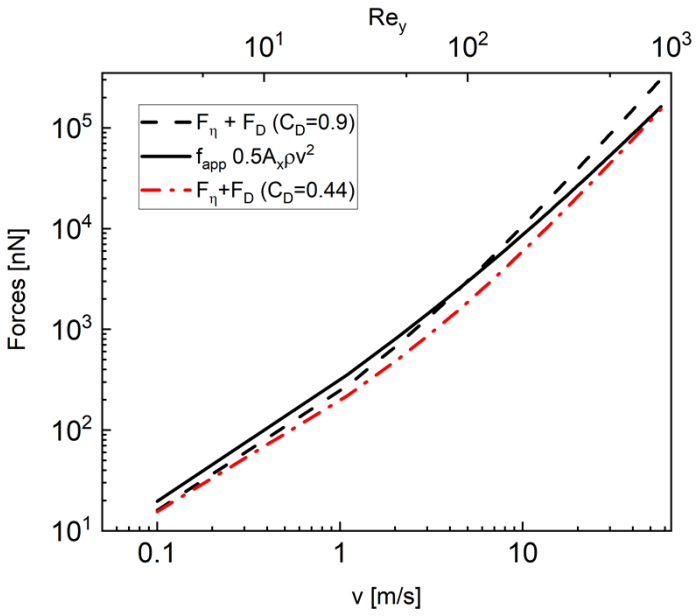

Fig. SI17. *Simulation of the total force that the fluid exerts on a sphere of radius* $\frac{D}{2} = 4\mu m$*, in water* ($\eta = 10^{-3} Pa \cdot s$) *as a function of the fluid speed* v *and of the Reynolds number* $Re_y = \frac{\rho_{fl} v D}{\eta}$ ($\rho_{fl} = 10^3 \frac{kg}{m^3}$). *The solid black line corresponds to the "true" force obtained as* $F \simeq \left(\sqrt{\frac{24}{Re_y}} + 0.5407\right)^2 \pi \left(\frac{D}{2}\right)^2 0.5 \rho_{fl} v^2$*. The black dashed and the red dot-dashed lines report the total fluid force on the tip approximated as* $F_{tip} = F_\eta + F_\rho = fv + \frac{C_D}{2} \rho_{fl} A_x v^2$*, with* $C_D = 0.9$ *and* $C_D = 0.44$*, respectively.*

It is noteworthy that the approximation of F_{tip} with $C_D = 0.44$, appropriate for a sphere (**Fig.SI16**, red dot-dashed line), underestimates systematically the correct value of the fluid force (**Fig.SI16**, solid line) and approaches asymptotically the viscous and the drag cases for low and high values of the Reynolds number, respectively. On the other hand, the approximated expression of the force that we compute for $C_D = 0.9$ (Fig.SI16, dashed black line), approximates the true value by $\pm 14\%$ for a range $5 \leq Re_y \leq 150$, as investigated here, while it overestimates it for larger values of the Reynolds number.

A better description of the total fluid force in the intermediate Reynolds number regime should resort to numerical simulations, but in the present work we will resort to the approximation $F_{tip} = F_\eta + F_\rho = fv + \frac{C_D}{2}\rho_{fl}A_x v^2$.

11. Bibliography

1 C. A. Marquezin, N. G. Ceffa, F. Cotelli, M. Collini, L. Sironi and G. Chirico, *Anal. Chem.*, 2016, **88**, 7115–7122.

2 M. J. Rossow, W. W. Mantulin and E. Gratton, *J. Biomed. Opt.*, 2010, **15**, 026003.

3 F. P. Beer, E. R. Johnston, J. T. DeWolf and D. F. Mazurek, *Mechanics of Materials*, McGraw Hill, 8th edn., 2020.

4 Doi M.; Edwards S.F., *The theory of polymer dynamics*, Oxford : Clarendon Press, 1986.

5 J. L. Hutter and J. Bechhoefer, *Rev. Sci. Instrum.*, 1993, **64**, 1868–1873.

6 R. Lévy and M. Maaloum, *Nanotechnology*, 2002, **13**, 33–37.

7 S. Große, T. Soodt and W. Schröder, *Meas. Sci. Technol.*, 2008, **19,105201**, 1–12.

8 M. M. Rahman, M. M. Karim and M. A. Alim, *J. Nav. Arch.* , 2007, **4**, 1813–8535.

9 U. Fey, M. König and H. Eckelmann, *Phys. Fluids*, 1998, **10**, 1547–1549.

10 S. Zhang, N. Cagney, S. Balabani, C. P. Naveira-Cotta and M. K. Tiwari, *Phys. Fluids*, 2019, **31**, 1–12.

11 F. Burla, Y. Mulla, B. E. Vos, A. Aufderhorst-Roberts and G. H. Koenderink, *Nat. Rev. Phys.*, 2019, 1, 249–263.

12 T. Hána, T. Janda, J. Schmidt, A. Zemanová, M. Šejnoha, M. Eliášová and M. Vokáč, *Materials (Basel).*, 2019, **12**, **2241**, 1–20.

13 W. Coffey and Kalmykov Yu P, *The Langevin equation : with applications to stochastic problems in physics, chemistry and electrical engineering*, World Scientific Publishing Co. Pte. Ltd., Singapore ; Hackensack, N.J., 2017, vol. 28.

14 M. J. Shelley and J. Zhang, *Annu. Rev. Fluid Mech.*, 2011, **43**, 449–465.

15 F. Yan, H. Yang and L. Wang, *Water (Switzerland)*, 2021, **13**, 1–22.

16 H. Bruus, *Theoretical Microfluidics. 2008*, Oxford University press, new york, 2008.

17 I. Proudman and J. R. A. Pearson, *J. Fluid Mech.*, 1957, **2**, 237–262.

18 R. B. Bird, E. N. Lightfoot and W. E. Stewart, *Transport Phenomena*, John Wiley & sons, New York, 2002.

19 J. N. Tilton, *Perry's Chemical Engineers' Handbook*, Mc Graw Hill, Educational, New York, 9th edn., 2019.